Analysis of Minimum-Variance and Wiener-Filtered Beamforming Strategies

Nghia Q. Nguyen,[a,c] Craig K. Abbey,[d] and Michael F. Insana[a,b,c]
[a]Department of Electrical and Computer Engineering, [b]Department of Bioengineering
[c]Beckman Institute for Advanced Science and Technology,
University of Illinois at Urbana-Champaign, USA
[d]Department of Psychology and Brain Sciences, University of California, Santa-Barbara, USA

***Abstract*— We show that the minimum-variance (MV), Wiener-filtered (WF), and other beamformers can be derived as approximations to the ideal-observer's strategy for lesion feature discrimination. We analyze breast lesion discrimination performance for five beamformers. Four of the five include matching filtering of receive-channel signal before summation, because there is no loss of task information in the RF signals due to this beamforming. Differences among beamformers occur depending on how they prepare RF signals for demodulation. Generally the MV and WF beamformers decorrelate the echo signals the most before demodulation, which transfers more task information into the B-mode data. We find the WF beamformer performs better than others because it is the closest approximation to the ideal observer strategy. The MV beamformer requires an additional low-rank approximation that handicaps performance for discriminating four of the five lesion features, but performs well for the fifth task because reducing rank filters data that is well matched to the task 5 feature spectrum. However, similarly reducing the rank of the WF filter makes it the beamformer of choice.**

Index Terms - breast cancer, ideal observer, task-based design

I. Introduction

The computational speed and configuration flexibility of current digital beamformers in medical sonographic systems now make it realistic to consider implementing more complex alternatives to the current standard of delay-and-sum (DS) beamforming. Several research groups have applied the minimum-variance (MV) beamformer to sonography that was pioneered by Capon and Frost for other applications, and they found improvements in spatial and contrast resolutions [1], [2]. The MV beamformer selects receive-channel filters that minimize the weighted array power output in all directions except along the beam axis. Recently, Nisel et al. [3] described a Wiener-filter (WF) beamforming approach, which minimizes the mean-squared error instead of the variance. The WF beamformer further improved contrast resolution compared with the MV approach, especially under low echo-signal-to-noise (eSNR) conditions. Although both were shown to improve image metrics, there remains a larger question of how to predict the performance of any beamformer for achieving diagnostic objectives.

We propose using ideal Bayesian observer analysis as a basis for beamformer design and evaluation. This paper builds on our initial development [4]. In this report, we derive the MV and WF approaches from the test statistic of the ideal observer to evaluate their relative performances for the task of discriminating breast lesion features. One advantage of the ideal observer methodology is its ability to relate sonographic instrument properties (resolution and noise figures) directly to observer performance for features that can be specified exactly [5], [6]. Observers are trained humans or algorithms that evaluate criteria according to the rules of decision theory. Another advantage of this approach is the ability to track task information flow through the image formation and diagnostic processes. Since the ideal observer provides an upper bound for task performance, comparisons with practical-observer performance defines the efficiency of an imaging instrument for delivering task information to observers.

In this paper, we show that MV and WF beamformers can be expressed as different approximations to the ideal observer strategy. Both apply a matched filter to each receive-channel signal that is composed of the channel's pulse-echo impulse response. After summation, each method filters the beamformed RF echoes prior to envelope detection, but the filters are different because they reflect the minimum variance versus minimum mean-squared error strategies. The performance of both beamformers was measured for five discrimination tasks involving breast lesion features. The results varied predictably depending on the nature of the task and on how well each beamformer was able to approximate the strategy of the ideal observer for that task.

II. Methods

A. Analysis.

Sonograms are formed in two stages. Acquisition yields the formation of beamformed RF echo signals and display results in the formation of the B-mode image. These are described, respectively, by the following three equations [5], [6],

$$\mathbf{g} = \mathbf{H}\mathbf{f} + \mathbf{n}\,, \quad \mathbf{g}_{\mathrm{BF}} = \mathbf{B}\mathbf{g} \qquad \text{and} \qquad \mathbf{b} = \mathcal{O}\mathbf{g}_{\mathrm{BF}}\,. \quad (1)$$

$\mathbf{f}$, $\mathbf{g}$, $\mathbf{g}_{\mathrm{BF}}$, and $\mathbf{b}$ are vectors describing backscatter in the object, pre- and post-beamformed RF echo data, and B-mode image of the object being examined, respectively. They are each discrete 2-D signals arranged into column vector by lexicographical reordering. $\mathbf{n}$ is acquisition noise of the

system, $\mathbf{H}$ is a linear system matrix mapping object scattering in the spatial domain to echo data in the time domain, and $\mathbf{B}$ is the operation of channel summing resulting in beamformed RF signals. Finally $\mathcal{O}$ is a nonlinear image reconstruction operator that converts RF data into B-mode images.

We represent RF signals from each receive channel by

$$\mathbf{g} = \begin{bmatrix} \mathbf{g}_0 \\ \mathbf{g}_1 \\ \vdots \\ \mathbf{g}_{N-1} \end{bmatrix} = \begin{bmatrix} \mathbf{H}_0 \\ \mathbf{H}_1 \\ \vdots \\ \mathbf{H}_{N-1} \end{bmatrix} \mathbf{f} + \begin{bmatrix} \mathbf{n}_0 \\ \mathbf{n}_1 \\ \vdots \\ \mathbf{n}_{N-1} \end{bmatrix} = \mathbf{H}\mathbf{f} + \mathbf{n} \ , \quad (2)$$

where $\mathbf{g}_j$ is the RF echo signal from element $0 \leq j \leq N-1$. $\mathbf{H}_j$ describes the transmit aperture characteristics and receive properties of the j^{th} receive channel. Channel acquisition noise $\mathbf{n}_j$ is modeled as a zero-mean white Gaussian process with variance σ_{n}^2. As $\mathbf{B}$ is the operation that sums echo signals across receiver channels, we can write the beamformed RF signal as

$$\mathbf{g}_{\text{BF}} = \mathbf{H}_{\text{BF}}\mathbf{f} + \mathbf{n}_{\text{RF}} \ , \ \text{where} \ \ \mathbf{H}_{\text{BF}} = \mathbf{B}\mathbf{H} \ \ \text{and} \ \ \mathbf{n}_{\text{BF}} = \mathbf{B}\mathbf{n} \ .$$

Each lesion feature has a unique benign-malignant signature pair that are labeled $i = 0$ or 1, respectively. The probability density function (pdf) of object scattering for the i^{th} class of data is modeled by a zero-mean, uncorrelated, nonstationary, multivariate normal process:

$$p_i(\mathbf{f}) = \mathcal{N}(\mathbf{0}, \sigma_{\text{obj}}^2(\mathbf{I} + \mathbf{S}_i)) \ \text{ for } i = 0, 1 \ . \quad (3)$$

$\sigma_{\text{obj}}^2(\mathbf{I} + \mathbf{S}_i))$ is the covariance matrix, $\mathbf{I}$ is the identity matrix, and diagonal matrix $\mathbf{S}_i$ defines deviations in uniform background tissue scattering that specify features of the i^{th} class. Diagnostic information about lesion features is contained in the covariance.

The pdf for $\mathbf{g}_i$ corresponding to $\mathbf{f}_i$ are

$$\begin{aligned} p_i(\mathbf{g}) &= \mathcal{N}(\mathbf{0}, \Sigma_i) \ \text{ for } i = 0, 1 \ , \text{where} \\ \Sigma_i &= \sigma_{\text{obj}}^2 \mathbf{H} \left(\mathbf{I} + \mathbf{S}_i\right) \mathbf{H}^t + \sigma_{\text{n}}^2 \mathbf{I} \end{aligned} \quad (4)$$

is the covariance matrix of the echo signals. eSNR is adjusted by varying the echo strength via σ_{obj}^2.

The ideal observer's strategy for distinguishing the two classes of data is described by a test statistic given as the log-likelihood ratio,

$$\lambda(\mathbf{g}) = \ln \frac{p_1(\mathbf{g})}{p_0(\mathbf{g})} \longrightarrow \mathbf{g}^t(\Sigma_0^{-1} - \Sigma_1^{-1})\mathbf{g} \ . \quad (5)$$

The right side of (5) is formed by eliminating terms that do not depend on $\mathbf{g}$. Larger values of λ indicate a greater likelihood for class 1 condition than class 0. Applying this strategy guarantees optimal performance under the assumptions.

We also use the *Smith-Wagner (SW) observer* as the ideal observer on B-mode images $\mathbf{b}$. The SW observer test statistic is given by [7]

$$\lambda_{\text{SW}}(\mathbf{b}) = \mathbf{b}^t(\mathbf{S}_1 - \mathbf{S}_0)\mathbf{b} \ . \quad (6)$$

The performance of ideal and SW observer is calculated numerically through Monte-Carlo studies. Details of those studies are provided in [4]–[6].

B. Approximations to the Ideal Observer Strategy

The beamforming strategy of the ideal observer is hidden within the compact express of (5). We can obtain insights by applying the *Woodbury matrix inverse identity* [8] to the inverse of covariance matrices as given by,

$$(\mathbf{A} + \mathbf{B}\mathbf{C}\mathbf{D})^{-1} = \mathbf{A}^{-1} - \mathbf{A}^{-1}\mathbf{B}(\mathbf{C}^{-1} + \mathbf{D}\mathbf{A}^{-1}\mathbf{B})^{-1}\mathbf{D}\mathbf{A}^{-1} \ , \quad (7)$$

provided matrices $\mathbf{A}$ and $\mathbf{C}$ are invertible.

Applying (7) to the expression for Σ_i^{-1} in (4), we obtain

$$\Sigma_i^{-1} = \sigma_{\text{n}}^{-2}\mathbf{I} - \sigma_{\text{obj}}^2\sigma_{\text{n}}^{-2}\mathbf{H}\left((\mathbf{I} + \mathbf{S}_i)^{-1} + \mathbf{K}_{\text{n}}\right)^{-1}\sigma_{\text{n}}^{-2}\mathbf{H}^t \ , \quad (8)$$

where $\mathbf{K}_{\text{n}} \triangleq \sigma_{\text{obj}}^2\mathbf{H}^t\mathbf{H}/\sigma_{\text{n}}^2$. Consequently, the test statistic is

$$\lambda(\mathbf{g}) = \sigma_{\text{obj}}^2\sigma_{\text{n}}^{-2}\mathbf{g}^t\mathbf{H}\left(\Psi_1^{-1} - \Psi_0^{-1}\right)\mathbf{H}^t\mathbf{g}\sigma_{\text{n}}^{-2} \ , \quad (9)$$

where $\Psi_i = (\mathbf{I} + \mathbf{S}_i)^{-1} + \mathbf{K}_{\text{n}}$.

The expanded expression for $\lambda(\mathbf{g})$ in (9) reveals the ideal strategy for beamforming. The first step is to calculated $\mathbf{H}^t\mathbf{g}$ and $\mathbf{g}^t\mathbf{H}$, which combine matched filtering on each receive channel signal with a summation across channels. We showed this irreversible process preserves the information in the RF echo signal [4], but there is no guarantee the information will survive the B-mode display stage in a form accessible by observers. In fact, we measured a significant loss of task performance if the envelope image is computed immediately after matched filtering [4]. Let's continue to explore the other factors involved with the ideal observer's strategy.

Assuming $\mathbf{K}_{\text{n}}$ or $\mathbf{H}^t\mathbf{H}$ is invertible, we apply (7) to Ψ_i and find

$$\Psi_i^{-1} = \mathbf{K}_{\text{n}}^{-1} - \mathbf{K}_{\text{n}}^{-1}\left(\mathbf{K}_{\text{n}}^{-1} + \mathbf{I} + \mathbf{S}_i\right)\mathbf{K}_{\text{n}}^{-1} \ . \quad (10)$$

Substituting (10) into (9), we obtain

$$\lambda(\mathbf{g}) = \sigma_{\text{obj}}^2\sigma_{\text{n}}^{-2}\mathbf{g}^t\mathbf{H}\mathbf{K}_{\text{n}}^{-1}(\mathbf{\Phi}_0^{-1} - \mathbf{\Phi}_1^{-1})\sigma_{\text{n}}^{-2}\mathbf{K}_{\text{n}}^{-1}\mathbf{H}^t\mathbf{g} \ , \quad (11)$$

where $\mathbf{\Phi}_i = \mathbf{K}_{\text{n}}^{-1} + \mathbf{I} + \mathbf{S}_i$, i = 0 or 1.

The ideal observer test statistic in (11) can be explored further by adopting the first-order approximation of $(\mathbf{I} + \mathbf{A})^{-1} \simeq \mathbf{I} - \mathbf{A}$ to calculate, $\mathbf{\Phi}_i^{-1}$ [5], where $\mathbf{A} \triangleq \mathbf{K}_{\text{n}}^{-1} + \mathbf{S}_i$:

$$\begin{aligned} \mathbf{\Phi}_i^{-1} &\simeq \mathbf{I} - (\mathbf{K}_{\text{n}}^{-1} + \mathbf{S}_i) \ \text{ and} \\ \lambda(\mathbf{g}) &\simeq \sigma_{\text{obj}}^2\sigma_{\text{n}}^{-2}\mathbf{g}^t\mathbf{H}{\mathbf{K}_{\text{n}}}^{-1}(\mathbf{S}_1 - \mathbf{S}_0)\sigma_{\text{n}}^{-2}{\mathbf{K}_{\text{n}}}^{-1}\mathbf{H}^t\mathbf{g} \end{aligned} \quad (12)$$

The first-order approximation in (12) describes filtered echo signals $\sigma_{\text{n}}^{-2}{\mathbf{K}_{\text{n}}}^{-1}\mathbf{H}^t\mathbf{g}$ that are squared and multiplied by the task difference $\Delta\mathbf{S} = \mathbf{S}_1 - \mathbf{S}_0$. Since $\Delta\mathbf{S}$ is a diagonal matrix, $\lambda(\mathbf{g})$ is not changed if we replacing $\sigma_{\text{n}}^{-2}{\mathbf{K}_{\text{n}}}^{-1}\mathbf{H}^t\mathbf{g}$ by its envelope. Comparing this result to the form of Smith-Wagner observer in (6), we interpret $\sigma_{\text{n}}^{-2}{\mathbf{K}_{\text{n}}}^{-1}\mathbf{H}^t\mathbf{g}$ as helping to preserve the ideal observer's test statistic as it passes through demodulation. Thus, ideal performance or task information is maximized at the display stage. This interpretation is accurate provided the first-order approximation in (12) is valid.

With $\mathbf{K}_{\text{n}}$ given in (8), the term $\sigma_{\text{n}}^{-2}{\mathbf{K}_{\text{n}}}^{-1}\mathbf{H}^t\mathbf{g}$ is recognized as the *Generalized Sidelobe Canceller* (GSC) or *Frost* beamformer of the RF data $\mathbf{g}$ [9]. It is the MV beamformer when the element impulse responses are known. In our analysis,

known impulse responses were required to model the ideal observer for the condition of signal known statistically. It explains the difference between the MV beamformer derived in this analysis and that from [1], [2].

The validity of the first-order approximation in (12) can be poor under low eSNR conditions; i.e., the eigenvalues of $\mathbf{K}_{\mathrm{n}}^{-1}$ are large. To improve the approximation, we use a new decomposition of $\mathbf{\Phi}_i = (\mathbf{K}_{\mathrm{n}}^{-1} + \mathbf{I}) + \mathbf{S}_i$. Consequently,

$$\begin{aligned} \mathbf{\Phi}_i^{-1} &\approx (\mathbf{K}_{\mathrm{n}}^{-1} + \mathbf{I})^{-1} - (\mathbf{K}_{\mathrm{n}}^{-1} + \mathbf{I})^{-1}\mathbf{S}_i(\mathbf{K}_{\mathrm{n}}^{-1} + \mathbf{I})^{-1} \quad \text{and} \\ \lambda(\mathbf{g}) &\approx \sigma_{\mathrm{obj}}^2\sigma_{\mathrm{n}}^{-2}\mathbf{g}^t\mathbf{H}(\mathbf{K}_{\mathrm{n}} + \mathbf{I})^{-1} \\ &\times (\mathbf{S}_1 - \mathbf{S}_0)\sigma_{\mathrm{n}}^{-2}(\mathbf{K}_{\mathrm{n}} + \mathbf{I})^{-1}\mathbf{H}^t\mathbf{g}\,. \end{aligned} \tag{13}$$

Similarly, $\sigma_{\mathrm{n}}^{-2}(\mathbf{K}_{\mathrm{n}} + \mathbf{I})^{-1}\mathbf{H}^t\mathbf{g} = (\sigma_{\mathrm{obj}}^2\mathbf{H}^t\mathbf{H} + \sigma_{\mathrm{n}}^2\mathbf{I})^{-1}\mathbf{H}^t\mathbf{g}$ helps preserve task information through the demodulation process of display. It is the Wiener filter beamformer [9]. This form also requires the assumption that the first-order approximation (13) is accurate.

We showed above that MV and WF beamformers are both approximations of the ideal strategy. In both cases, they spatially decorrelate the RF echo signals before demodulation, which preserves more task information as compared with the delay-and-sum (DS) and matched filter (MF) beamformers. Before measuring discrimination efficiencies as described below, we predict that the WF beamformer should outperform the MV beamformer based solely on the observation that WF is a better approximation to the ideal observer strategy for low eSNR. In the visual discrimination efficiencies shown below, values close to one mean that the SW observer of the B-mode image performs equivalently to the ideal observer of the RF echo signal, and therefore all task information is transferred into the image. The caveat is that we do not know the performance of the SW observer relative to the human observer except for Task 1.

The requirement that the inverse of $(\mathbf{H}^t\mathbf{H})$ exist and be well conditioned challenges the experimental validation of our analysis. A full treatment of this issue is beyond the scope of this conference paper but a brief discussion of these important computational issues is given below.

C. Discrimination Tasks.

Through discussions with a radiologist, we identified five features of breast lesions commonly sought to visually differentiate benign lesions from malignant ([5], Fig. 2). Task 1 is detection of low-contrast hypoechoic lesions; Task 2 is discrimination of an elongated eccentric lesion from a circular lesion; Task 3 is discrimination of a soft, poorly defined boundary from a well circumscribed lesion; Task 4 is discriminating boundary irregularities (spiculations) from a well-circumscribed lesion; and Task 5 is discriminating a very weakly scattering hypoechoic interior from an anechoic interior. Task difficulty is controlled through contrast parameter C that governs the difference between variance maps $\mathbf{S}_i$ for the two classes. C is defined in [5].

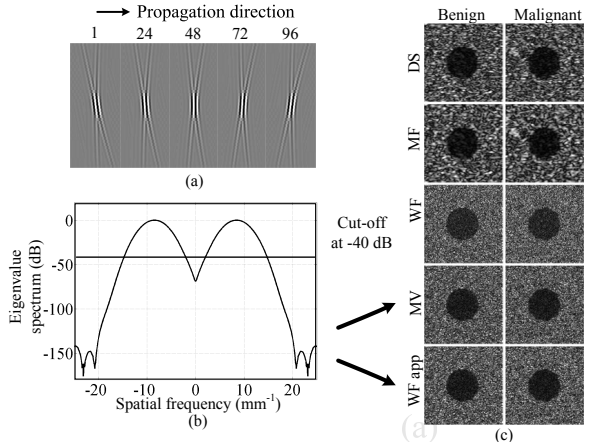

Fig. 1. (a) The impulse responses from receiver channels generated with Field II [10]. (b) The normalized eigenvalue spectrum of $\mathbf{H}^t\mathbf{H}$ with a cutoff at -40 dB to implement the MV beamformer. (c) Example pair of B-mode images for task 4 using the beamformers DS, MF, WF, MV, and WFapp. The latter method is WF with the same low-rank approximation applied to MV.

III. Results

Examples of image simulations are found in Fig. 1. Pulse echo psfs at the receive channel in Fig. 1(a) are generated by using the Field II program [10], with parameters from the Siemens Sono-line Antares system and the VF 10-5 linear array transducer [6].

The number active tx-rx elements 96. Based on the psfs of those element, we implemented DS, MF, WF and MV beamformers. Since $\mathbf{H}$ has a very large size, a circulant assumption was made for each $\mathbf{H}_j$ providing advantages in computation [5]. The MV beamformer involves the ill-conditioned matrix product $(\mathbf{H}^t\mathbf{H})^{-1}$, which requires a low-rank approximation. Fig. 1(b) shows the normalized eigenvalue spectrum of $\mathbf{H}^t\mathbf{H}$. By cutting-off frequency contributions less than -40 dB, the MV is implemented as the pseudoinverse of $\mathbf{H}$ [9]. Since system modeling is changed slightly with the low-rank approximation, we also implemented the WF beamformer with the same low-rank approximation for comparisons and refer to it as WFapp.

Fig. 1(c) shows an example of B-mode images for Task 4 with the spiculated "malignant" lesion on the right in all cases. Among the 5 beamformers, the MF beamformer has the largest speckle. The effects of the WF and MV beamformers are to reduce speckle sizes and clarify lesion boundaries. Visually comparing WF and MV images, WF appears to have a better spatial resolution but lower contrast resolution. The WF beamformer with the low-rank approximation (WFapp) appears to have a spatial resolution on par with the MV and a somewhat improved contrast resolution.

Beamformer performance is quantified using observer efficiency that, in this case, characterizes the loss of task information through demodulation. The efficiency is calculated by

$$\eta = \left(\frac{C_I}{C_{SW}}\right)^2, \tag{14}$$

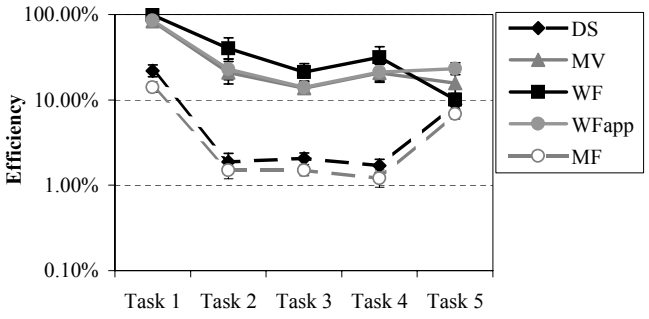

Fig. 2. Observer efficiencies on B-mode images with different beamformers. An efficiency of 1 indicates that all task information is passed from RF echo signals into B-mode images. Error bars indicate one standard error.

where C is the contrast factor for a feature and subscripts SW and I refer to values obtained from SW and ideal observers.

The efficiencies of the 5 beamformers applied to 5 lesion features are plotted in Fig. 2. The efficiency of MF is always the lowest. The WF and MV make substantial improvements for the first four tasks, but in Task 5 (anechoic/hypoechoic), the efficiency of WF is reduced to approximately that of the DS (10.08% vs 8.85%). In Task 5, efficiency for MV is larger (15.71%), however, the WFapp outperforms all others. The improvement of WFapp in comparison with the MV is very small in the first four tasks (less than 2%) but significant Task 5 (7.45%). To compare with the WF full rank, WFapp has lower efficiency in the first four tasks, but higher in Task 5 (23.16% vs 10.08%).

IV. Discussions

We found by applying ideal observer analysis that the minimum variance (MV) and Wiener filter (WF) beamformers are each approximations to the ideal strategy. In forming B-mode imaging, there are two irreversible processes that reduce task information. The first loss occurs in beamforming at the acquisition stage, and the second loss occurs in demodulation at the display stage. While beamforming compresses signals from multiple elements within an aperture, demodulation discards the phase component of RF data as required to interface with the human eye-brain system.

In [4], we found that the MF beamformer preserves task information transferred from the receive channels to the beamformed RF echo signals. However, the MF beamformer results in a relatively large loss of task information during demodulation. Observer efficiency for MF is the lowest for all five visual tasks. In this study, we found that MF should be followed by de-blurred operations, which occur with the WF and MV beamformers. De-blurring helps preserve task information through demodulation. Visually, these beamformers reduce the speckle sizes and clarify the lesion definition at the boundaries. Both beamformers improve SW observer efficiency.

The difference between WF and MV beamformers is the term $\sigma_{\mathrm{n}}^2\mathbf{I}$. The importance of the term comes from the requirement for accurate first-order approximation to the covariance matrix inverse. The better approximation of the WF beamformer improves the SW observer performance. Therefore WF should outperforms MV in all five tasks. The improvement is significant when $(\sigma_{\mathrm{obj}}^2\mathbf{H}^t\mathbf{H}/\sigma_{\mathrm{n}}^2)^{-1}$ has large eigenvalues (low eSNR). This finding agrees with the results from [3] but ours is based on the ideal observer formalism. Implementation of the MV, however, requires a low-rank approximation that changes the system model. To compare the two beamformers, we apply the same low-rank approximation to give the WFapp beamformer. The results show that the efficiencies of WFapp are higher than those of MV in all five tasks as predicted from the analysis. Compared to WF, the efficiency of WFapp is lower in the first four tasks but higher in Task 5. This finding is explained by noting that the noise filtering advantages of rank reduction are well matched to the spatial-frequency requirements of Task 5.

Since approximations are adopted that may reduce the potential gains in task performance, the final results should be evaluated using human observer studies. Also the SW observer is a reliable performer for Task 1 but only approximate for other tasks. It is possible that improvements in the SW observer performance, or perhaps develop of a model observer that response similar to human observers, will modify these efficiencies somewhat, as it has in our previous studies [5], [6].

Acknowledgment

This work is supported by NIH under award No. CA118294.

References

[1] Z. Wang, J. Li, R. Wu, "Time-delay- and time-reversal-based robust Capon beamformers for ultrasound imaging," *IEEE Transactions on Medical Imaging*, vol. 24, pp. 1308-1322, Oct. 2005.

[2] J.-F. Synnevåg, A. Austeng, and S. Holm, "Adaptive beamforming applied to medical ultrasound imaging," *IEEE Transactions on Ultrasonics, Ferroelectrics, and Frequency Control*, vol. 54, no. 8, pp. 1606-1613, Aug. 2007.

[3] C.-I. C. Nilsen and S. Holm, "Wiener Beamforming and the Coherence Factor in Ultrasound Imaging," *IEEE Transactions on Ultrasonics, Ferroelectrics, and Frequency Control*, vol. 57, no. 6, pp. 1329-1346, Jun. 2010.

[4] C.K. Abbey, N.Q. Nguyen, M.F. Insana, "Optimal beamforming in ultrasound using the ideal observer," *IEEE Trans Ultrason Ferroelectr Freq Control*, vol. 57, no. 8, pp. 1782-1796, August, 2010.

[5] C.K. Abbey, R.J. Zemp, J. Liu, K.K Lindfors, M.F. Insana, "Observer efficiency in discrimination tasks simulating malignant and benign breast lesions with ultrasound," *IEEE Transactions on Medical Imaging*, vol. 25, no. 2, pp. 198-209, Feb. 2006.

[6] N.Q. Nguyen, C.K. Abbey, M.F. Insana, "An adaptive filter to approximate the Bayesian strategy for sonographic beamforming," *IEEE Trans Med Imag*, vol. 30, no. 1, pp. 28-37, Jan. 2011.

[7] S.W. Smith, R.F. Wagner, J.M. Sandrik, and H. Lopez, "Low contrast detectability and contrast/detail analysis in medical ultrasound," *IEEE Trans Son Ultrason*, vol. 30, no. 3, pp. 164-173, May 1983.

[8] H.H. Barrett and K.J. Myers, *Foundations of Image Science*. Hoboken, NJ: John Wiley & Sons, 2004.

[9] H.L. Van Trees, *Detection, Estimation, and Modulation Theory, Part IV, Optimum array processing*. New York, NY: Wiley, 2002.

[10] J.A. Jensen and N.B. Svendsen, "Calculation of pressure fields from arbitrarily shaped, apodized, and excited ultrasound transducers," *IEEE Transactions on Ultrasonics, Ferroelectrics, and Frequency Control*, vol. 39, no. 2, pp. 262-267, 1992.